Soil Dynamics and Earthquake Engineering 147 (2021) 106772

Contents lists available at ScienceDirect

Soil Dynamics and Earthquake Engineering

journal homepage: www.elsevier.com/locate/soildyn

Nonlinear seismic analysis of a train-tunnel-soil system and running safety assessment of metro vehicles

Junjie Li [a], Yunfeng Lou [b], Xun Yang [c], Xianlong Jin [a,*]

[a] State Key Laboratory of Mechanical System and Vibration, Shanghai Jiao Tong University, Shanghai, China
[b] Aerospace System Engineering Shanghai, Shanghai, China
[c] Changchun Institute of Optics, Fine Mechanics and Physics, Chinese Academy of Sciences, Changchun, China

ARTICLE INFO

Keywords:
Train-tunnel-soil system
Metro train
Earthquake excitation
Seismic response
Numerical simulation
Running safety
Penalty method

ABSTRACT

Since earthquakes would pose a serious threat to the safety of underground railway tunnels and subway trains, the seismic analysis of the subway tunnel and the metro train is essential for earthquake-resistant design and construction. This presented study aims to investigate the transient response of a train-tunnel-soil coupled system under various load conditions, and assess running safety of the moving train. Firstly, a simulation model of the train-tunnel-soil system was established, considering interactions between soil and tunnel, rail and train. Secondly, the numerical approaches employed in this paper were verified, and the tunnel-soil model was validated with the available test data. Finally, the nonlinear seismic response of the train-tunnel-soil system is investigated, and running safety indices of the subway vehicle are evaluated. Moreover, the effect of train speed and earthquake intensity on the running safety of the metro train is assessed. The numerical results reveal that compared to the moving-train load, the effect of earthquake action on the dynamic response of the subway tunnel is more prominent, resulting in a significant increase of the wheel-rail force and acceleration of the railway vehicle. Both earthquake loads and train speed have an impact on running safety indices, while the earthquake intensity has a more significant effect on the safety index of the metro vehicle. Moreover, it is worth noticing that with respect to the designed operational speed of 90 km/h for Nanjing Metro Line 10, the ability of the metro train to withstand earthquake excitation is no more than a maximum acceleration of 0.2 g.

1. Introduction

With the rapidly advancing of the urbanization process around the world, the increasing traffic of urban areas has been a global issue. More and more cities exploit underground space resources to address traffic problems in urban development. As underground railway traffic has become an indispensable part of city transportation, it does not take the safety of underground railway tunnels and subway trains too seriously. The security of earthquake-resistant structures is essential to underground engineering structures such as metro tunnels. In addition to the tunnel lining damage caused by earthquakes, earthquake excitation can pose a severe security risk to the running safety of moving trains as a train passing through a subway tunnel.

Determining the seismic response of the train-tunnel-soil coupled system is a complicated procedure consisting of the nonlinear behaviour of soil, the wheel-rail relationship and the soil-tunnel interaction condition. In recent years, on that note a large number of research work has been implemented to get a better insight into the dynamic response of the tunnel-soil system subjected to ground motions. Some researchers concentrated on the vibration analysis of the tunnel-soil system during an earthquake load. The results of shaking table tests under non-uniform earthquake excitation proposed by Chen et al. [1] reveal that the spatial distribution of earthquake excitation should be taken into account for the earthquake-resistant design of utility tunnel. Anastasopoulos et al. [2] adopted beam-spring element model to capture the seismic response of segmental tunnel lining, and the length and joint properties of the segment was discussed. Hatzigeorgiou et al. [3] presented a new three-dimensional finite element model of a soil-tunnel coupling system to investigate the soil-tunnel interaction under earthquakes. Gomes et al. [4] found that the stratification of the ground determined the dynamic response of shallow circular tunnels during an earthquake load. A new numerical procedure was proposed by Do et al. [5,6] to simulate the dynamic behaviour of the multi-segment linings subjected to earthquake excitation. The results reported by Fabozzi et al. [7] indicated that a

* Corresponding author.
E-mail address: jxlong@sjtu.edu.cn (X. Jin).

https://doi.org/10.1016/j.soildyn.2021.106772
Received 21 January 2020; Received in revised form 9 January 2021; Accepted 10 April 2021
Available online 6 May 2021
0267-7261/© 2021 Elsevier Ltd. All rights reserved.

proper constitutive law of the soil is vital to simulate the influence of soil-tunnel relationship on the nonlinear response of segmental tunnel linings subjected to an earthquake load.

Several studies took the moving train excitation as an independent load to simulate the vibration performance of the subway tunnel lining. The structure of the foundation and tunnel discretize by using the boundary element approach, and finite element method was adopted by Degrande et al. [8] to study the influence of the vibration induced by the subway vehicle. A 2.5D coupled finite element-boundary element model employed by Galvin et al. [9] concentrated on the ground displacement response induced by moving trains, and the numerical results of the simplified method were validated. A coupled periodic finite element-boundary element model was used to discuss the response of tunnel subjected to the excitation of a Thalys high-speed train in Ref. [10]. Andersen et al. [11] established the 2D and 3D models of the tunnel structure to analyze the vibration from railway tunnels, and the results derived from numerical simulation were validated with the experiment. They concluded that the accuracy and stability of the two-dimensional model were much lower than that of the three-dimensional model.

Some other published papers were related to the running safety assessment of the train vehicle. Tanabe et al. [12] employed a finite element model to simulate the dynamic interaction between a high-speed train and the track structure subjected to earthquake loads. Ju [13] investigated the derailment of the railway vehicle moving on bridge structures numerically, and it was found that a large pier stiffness could ensure the safety of railway vehicles under earthquakes. Xia et al. [14] presented that significant responses of a train-bridge coupling model during collision loads strongly threatened the running safety of high-speed railway vehicles. According to the seismic response of a train-bridge coupled model, Yang et al. [15] proposed critical speeds for running safety of the railway vehicle. The conclusions from the studies [12–15] reveal that the seismic variation has a significant effect on the running safety of moving trains.

Nevertheless, in most of the research work related to the tunnel-soil system, the existing studies in which laboratory experiments, theoretical analysis and numerical simulations were carried out to get a main insight into the seismic response of the tunnel structure without considering the effect of train excitation, instead the moving train load was taken as an independent load to simulate the vibration of the underground tunnel structure. On the other hand, earthquakes can pose a severe security threat to the safety of subway trains in the underground tunnel, while little research concerns the running safety of the subway vehicle due to earthquake action. Therefore, this paper develops a train-tunnel-soil coupled system to investigate the dynamic response of the tunnel and the railway vehicle under various load conditions, and running safety of the moving train is also evaluated in this work.

In this paper, using the finite element method, a full three-dimensional train-tunnel-soil model based on the subway tunnel in respect of Nanjing Metro Line 10 is established. The nominal orthotropic constants of the tunnel lining structure are verified by comparing the dynamic response of the load test regarding the equivalent lining and the segmental lining. And the penalty method is used to investigate the wheel-rail relationship and the interaction condition between tunnel and soil. Then, numerical simulations were performed to verify the wheel-set contact model, calibrated the equivalent lining model and validate a tunnel-soil coupling model. Furthermore, with respect to the train-tunnel-soil coupled model, the dynamic response of the tunnel and moving train has been simulated. In addition, the running safety of a moving railway vehicle passing through the subway tunnel during an earthquake has been studied in detail. Moreover, due to the enormous computational effort [16,17], the simulation is performed based on the high-performance computer Magic Cubic-II using LS-DYNA FE (finite element) code.

2. Methodology

2.1. Explicit dynamic analysis

As the schematic of a train-tunnel-soil system is illustrated in Fig. 1, the dynamic model consists of the train vehicle submodel, the tunnel submodel and the soil submodel, with the external excitation of an earthquake load applied at the bottom of the foundation.

The interaction between the rail and the tunnel is assumed to be bonded, and the equations of motion can be given by:

$$\begin{bmatrix} \mathbf{M}_{VV} & 0 & 0 \\ 0 & \mathbf{M}_{TT} & 0 \\ 0 & 0 & \mathbf{M}_{SS} \end{bmatrix} \begin{Bmatrix} \ddot{\mathbf{U}}_V \\ \ddot{\mathbf{U}}_T \\ \ddot{\mathbf{U}}_S \end{Bmatrix} + \begin{bmatrix} \mathbf{C}_{VV} & \mathbf{C}_{VT} & 0 \\ \mathbf{C}_{TV} & \mathbf{C}_{TT} & \mathbf{C}_{TS} \\ 0 & \mathbf{C}_{ST} & \mathbf{C}_{SS} \end{bmatrix} \begin{Bmatrix} \dot{\mathbf{U}}_V \\ \dot{\mathbf{U}}_T \\ \dot{\mathbf{U}}_S \end{Bmatrix} + \begin{bmatrix} \mathbf{K}_{VV} & \mathbf{K}_{TV} & 0 \\ \mathbf{K}_{VT} & \mathbf{K}_{TT} & \mathbf{K}_{TS} \\ 0 & \mathbf{K}_{ST} & \mathbf{K}_{SS} \end{bmatrix} \begin{Bmatrix} \mathbf{U}_V \\ \mathbf{U}_T \\ \mathbf{U}_s \end{Bmatrix} = \begin{Bmatrix} \mathbf{F}_{VT} \\ \mathbf{F}_{TV} + \mathbf{F}_{TS} \\ \mathbf{F}_{ST} \end{Bmatrix} + \begin{Bmatrix} 0 \\ 0 \\ \mathbf{F}_E \end{Bmatrix} \tag{1}$$

Where the subscripts V, T and S denote the railway vehicle, the tunnel and the soil; $\mathbf{M}$, $\mathbf{C}$ and $\mathbf{K}$ represent mass, damping and stiffness matrices, respectively, $\ddot{\mathbf{U}}$, $\dot{\mathbf{U}}$ and U represent the acceleration, velocity and displacement vectors; $\mathbf{F}_{VT}$ and $\mathbf{F}_{TV}$ are internal force vector on the wheel-rail interface, while $\mathbf{F}_{TS}$ and $\mathbf{F}_{ST}$ are internal force vector on the tunnel-soil interface; $\mathbf{F}_E$ is the external force vector of the earthquake load.

As a metro train vehicle passes through the tunnel, the interaction forces on the interface between the underground subway tunnel and the train are always changing as a nonlinear formulation of the displacement, which leads to the time-varying coefficients placed before and multiplying the variable in the second-order linear non-homogeneous differential formulations of Eq. (1). For nonlinear engineering issues, only numerical simulations are possible. Thus, the Newmark iteration algorithm is adopted to integrate the equations of motion. An artificial hourglass resistance force is involved to avoid the hourglass deformation, and Eq. (1) at time t_n can be expressed as:

$$\mathbf{M}\ddot{\mathbf{U}}_n + \mathbf{C}\dot{\mathbf{U}}_n + \mathbf{F}_n^{\text{int}} = \mathbf{P}_n + \mathbf{H}_n \tag{2}$$

Where $\mathbf{M}$ represents the diagonal mass matrix, $\mathbf{F}_n^{int}$ denotes the stress divergence vector; $\mathbf{P}_n$ represents internal and external forces vector, $\mathbf{H}_n$ represents the hourglass-resistant force vector. The acceleration matrix at time t_n is obtained based on Eq. (2):

$$\ddot{\mathbf{U}}_n = \mathbf{M}^{-1}\left[\mathbf{P}_n - \mathbf{F}_n^{\text{int}} + \mathbf{H}_n - \mathbf{C}\dot{\mathbf{U}}_n\right] \tag{3}$$

As integrated by the explicit central difference scheme, velocity and displacement vectors are updated step by step to advance time t_{n+1}:

$$\begin{cases} \dot{\mathbf{U}}_{n+1/2} = \dot{\mathbf{U}}_{n-1/2} + \Delta t_n \ddot{\mathbf{U}}_n \\ \mathbf{U}_{n+1} = \mathbf{U}_n + \Delta t_{n+1/2}\dot{\mathbf{U}}_{n+1/2} \end{cases} \tag{4}$$

in which

$$\Delta t_{n+1/2} = (\Delta t_n + \Delta t_{n+1}) / 2 \tag{5}$$

The explicit integration algorithm adopts a diagonal mass matrix to enhance computational efficiency. However, the time step size determines the stability of the Newmark explicit integration proceeding, and the magnitude of the adopted time step is crucial to ensure accuracy. The time step can be given by Ref. [18]:

$$\Delta t \le \Delta t^{crit} = 2/\omega_{\max} = \min_e \frac{l_e}{c_e} \tag{6}$$

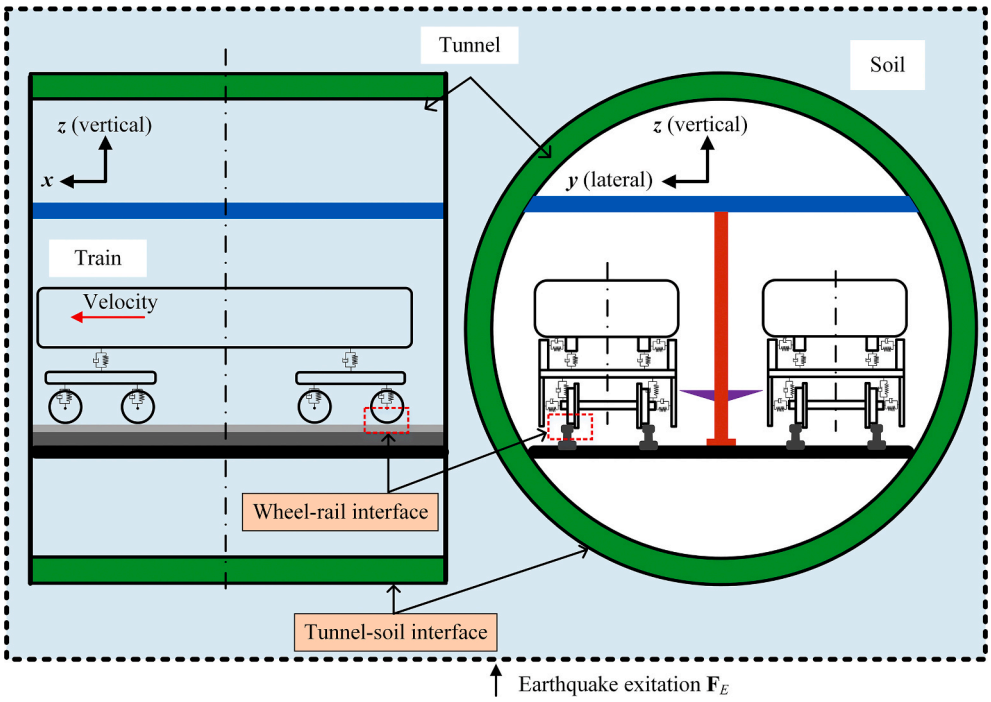

Fig. 1. Dynamic analysis model of the train–tunnel-soil system.

For nonlinear problems including damping, the time step size is described as [20]:

$$\Delta t \le \Delta t^{crit} = \frac{2}{\omega_{\max}}\left(\sqrt{1-\xi^2}-\xi\right) \tag{7}$$

where Δt^{crit} accounts for the critical time step. Parameters l_e and c_e are the characteristic length of the element and the sound speed, respectively. ω_{max} is the maximum circular frequency, and ξ is the damping ratio.

Therefore, the damping ratio reduces the magnitude of the critical time step. The value of time step is constrained by the largest natural frequency of structures which, in turn, is limited by the highest frequency of any individual element in the finite element model [18]. To reduce the destabilizing influence of nonlinearities, a scale factor for the time step is involved, and a new time step size by taking the minimum value over all elements is determined by:

$$\Delta t_{n+1} = T_s \times \min\left\{\Delta t^1, \Delta t^2, \cdots, \Delta t^N\right\} \tag{8}$$

Where T_s is the time step scale factor which is available from 0.67 to 0.9, Δt^N represents the time step size determined by the element, and N is the number of elements. The time step size roughly corresponds to the transient time of an acoustic wave through an element using the shortest characteristic distance [19]. In this paper, T_s equal to 0.8 is adopted to account for the stability during the integration of the highly nonlinear problem.

2.2. Wheel-rail contact

The wheel-rail contact problem is considerably complex. It can be formulated as a rolling contact problem between two nonlinear profiles in the presence of friction [20]. Regarding the dynamic analysis of a railway vehicle, the determination of the forces acting between wheel and track is exactly of the most importance.

In recent times, much effort and significant progress have been done to get more accurate and efficient formulations of wheel-rail contact model by many researchers [21–23]. The solution to the contact problem can be divided into four sub-problems:

1) the identification of the location of contact points between wheel-rail profiles;
2) normal forces acting between wheel and rail, evaluation of shape and dimension of the contact areas and the corresponding pressure distribution;
3) the relative motion of the wheel compared with the track;
4) tangential forces generated by friction and creepages in the contact area.

The wheel set moving along the track has a significant effect on the forces generated by the contact constraints due to the coupling of the two profiles. In addition, it makes the calculation far more complicated that track irregularities produce a variation along the track of the normal forces.

Considering the highly nonlinear characteristics of the wheel-rail contact model, the solution can be found only using numerical methods [20]. The symmetrical penalty function approach is employed to capture forces acting between wheel and rail. Fig. 2 illustrates the interaction relationship between the train vehicle and the track. The wheel segments represent the slave surface of the contact with the master nodes of the rail structure located at the wheel-rail interface. The wheel nodes are constrained to slide along the wheel-rail interface using the penalty equation.

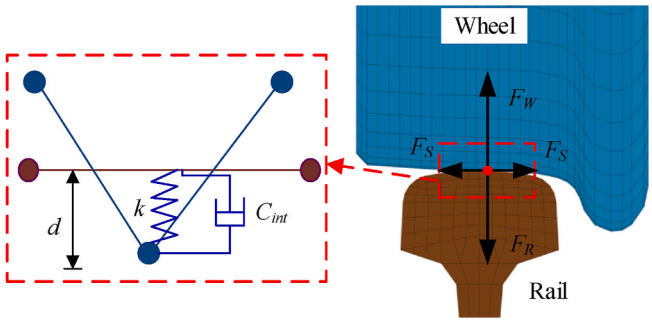

Fig. 2. Schematic sketch of wheel-rail contact.

The penalty function is used to capture the force acting on the wheel-rail interface. A linear force-deflection relationship is assumed in compression, and no tensile force is generated during the contact process [15]. As a penetration does occur, a normal contact force would be generated.

$$F_R = -F_W = k \cdot d + C_{\text{int}} \cdot \dot{d} \tag{9}$$

Where F_R and F_W represent normal contact force acting on the rail and the wheel, respectively; k represents the stiffness of spring. The parameter C_{int} denotes the damping coefficient, and d represents the penetration distance.

The tangential force F_S obeys the Mohr-Coulomb friction theory. The frictional force along the contact interface is calculated as follows [23].

$$F_S = \mu F_W + c\nu \tag{10}$$

Where parameters μ and c are friction coefficient and viscous damping, respectively. ν represents the relative sliding rate.

2.3. Soil constitutive law

The soil material constitutive law aims to describe the nonlinear relationship of the soil, such as the frictional resistance and the dilation angle. The criterions of Mohr-Coulomb (M − C) and Drucker-Prager (D-P) are the most wide-used nonlinear constitutive laws in soil dynamics [24]. In contrast to the M − C criterion, the yield surface of the D-P criterion adopted in this paper has no sharp angle, which has higher efficiency of numerical simulation, as shown in Fig. 3. Different circles represent different criteria of the yield surface on the deviator plane, and the yield criteria is selected according to the realistic definition for the soil during the specific dynamic simulation.

According to the Mohr-Coulomb yield criterion, the yield function of the Drucker-Prager criterion is expressed as:

$$f(\sigma) = \alpha I_1 + \sqrt{J_2} - k = 0 \tag{11}$$

Where $f(\sigma)$ represents the yield function, I_1 and J_2 denote the first and second invariants of the deviatoric stress tensor, respectively; α and k are material coefficients which are given by

$$\alpha = \frac{2\sin\varphi}{\sqrt{3}(3 \pm \sin\varphi)}, \quad k = \frac{6c\cos\varphi}{\sqrt{3}(3 \pm \sin\varphi)} \tag{12}$$

Where φ denotes the internal friction angle of the soil, and c denotes the cohesion of the soil. Parameters α and k determine the shape of the yield surface on the deviator plane illustrated in Fig. 3 above. The modified D-P model (*MAT_DRUCKER_PRAGER) was adopted in this study.

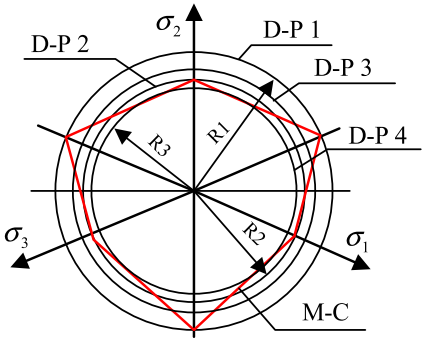

Fig. 3. The yield surface on the deviator plane.

2.4. Seismic excitation

Earthquake is one of the main natural disasters endangering human life and property and engineering structure safety. The amplitude of ground motion directly reflects the intensity of an earthquake, and the time history of seismic wave is usually given in the form of acceleration or displacement. The occurrence time of peak acceleration determines the effect of seismic loads on dynamic responses of the system. With respect to the seismic response analysis of the train-tunnel-soil coupling system, according to the speed and structure characteristics, the time of applying the ground motion load is adjusted to ensure that the train passes through the key concerned area when the ground motion reaches the peak value. In the present analysis, an actual observed seismic acceleration in Shanghai which is similar to underground railway system is adopted, as shown in Fig. 4. The duration of seismic excitation is 20 s with a peak acceleration of 0.496 g, which occurs at the time of 3.46 s.

3. Validation of numerical models

3.1. Verification of wheel-rail contact

3.1.1. Wheel-rail force under normal operation

A wheel-rail coupled model was established to verify the accuracy of the penalty function method for the wheel-rail contact. Fig. 5 shows the 3D model of the wheel-rail contact. The rails were composed of 8-node solid elements, and the fastener was represented as a linear spring damping element. The nodes at the bottom of the fastener structure were constrained. The irregularities of the track are neglected. A lumped mass of 14 tons is applied at wheel sets, and the wheels travel at a constant speed of 80 km/h.

Fig. 6 indicates the time history of the normal force acting between wheel and rail. It is obviously observed that after the initial balance in the first second, the vertical force is stable at 70 KN. During the period from 1 s to 5 s, the maximum, minimum and average value obtained from numerical simulation is 70.30 KN, 69.72 KN and 70.03 KN, respectively. Since the irregularities of the track are neglected, the theoretical force acting between wheel and rail is equal to 70 KN, determined by the gravity of lumped mass. The values of the simulation produce a maximum error of 0.52%.

3.1.2. Wheel-rail force at an obstacle encountered

In order to simulate the separation of the rail and wheel, with respect to the above case, an obstacle is introduced into the track where the wheel #2 moves along. As indicated in Fig. 7, the obstacle is a bump with a height of 10 mm and a length of 250 mm.

The wheel set is designed to encounter an obstacle at 3.93 s. Fig. 8 shows the running states of wheel sets at different times. After the wheel set passes through the obstacle, it is found that the wheel #1 and #2 separate from the rail, respectively. At the time of 4.4 s, there is an obvious separation between the wheel set and the rail, and the derailment takes place.

The profile of vertical contact force with separation between the wheel and the rail is shown in Fig. 9. As the wheel set encounters with

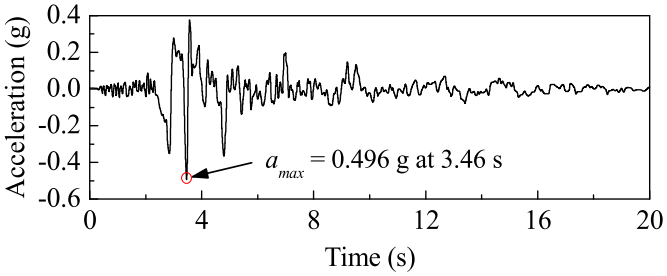

Fig. 4. Time history of actual observed seismic acceleration.

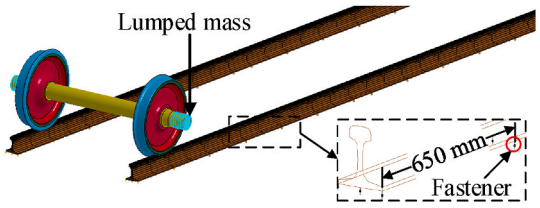

Fig. 5. FE model of wheel-rail contact.

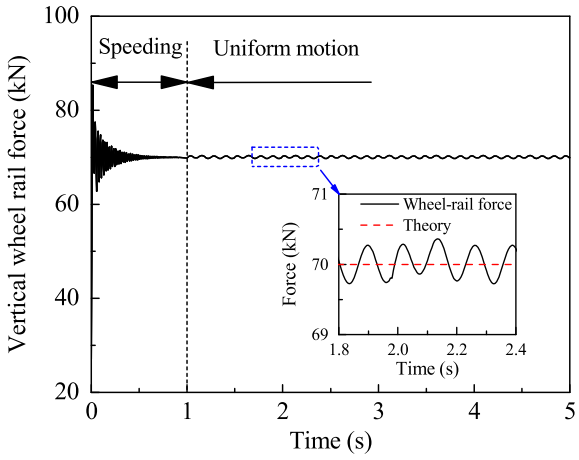

Fig. 6. Time history of vertical wheel-rail force.

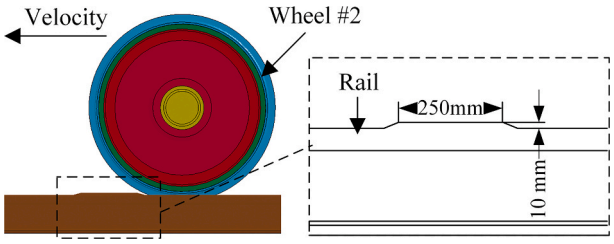

Fig. 7. Sketch map of an obstacle on a rail.

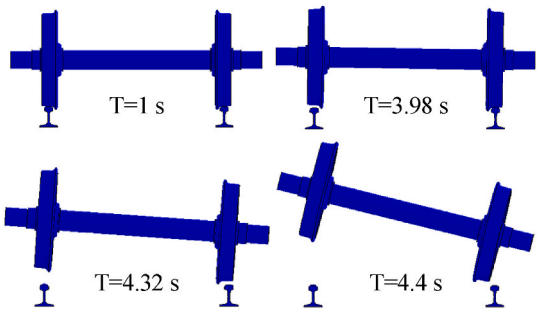

Fig. 8. Running states of wheel set at different times.

the obstacle in 3.93s, it has a significant impact on the vertical wheel-rail force, and there is a sharp fluctuation in the vertical contact forces of the wheel #1 as well as the wheel #2. The peak value of the vertical wheel-rail force is equal to 745 KN.

3.2. Calibration of the tunnel lining

In a typical underground subway tunnel, the lining component is connected with multiple segments. It proves difficult, complicated and

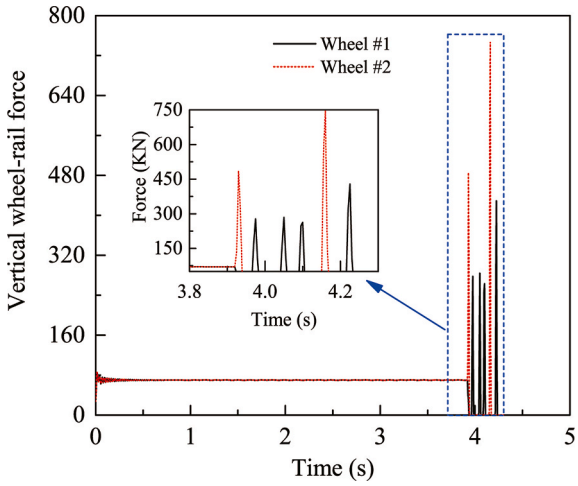

Fig. 9. Time history of vertical wheel-rail force under derailment.

time-consuming to model the nonlinear contact relationships and interactions between segments during conducting the dynamic simulation [25]. To improve computational efficiency without significant loss of accuracy, the tunnel structure is modeled instead of equivalent lining components. Fig. 10 shows the models of an 18-ring segmental lining and a continuous lining, and two models are the same in length, equal to 36 m.

The equivalent procedure is conducted to determine the nominal orthotropic constants of the equivalent continuous lining structure. Firstly, with the lining models shown in Fig. 10, the tunnel lining reduction simulations were performed to characterize proper initial values of material parameters for the equivalent lining model. The overburden load on the lining is generated by the gravity of the overburden soil, and the longitudinal load is assigned to the side of the linings. When the slopes of relationships of deformations and loads is consistent (see Fig. 11, red line and black line), initial material parameters of the equivalent lining were obtained. Secondly, the identification process of equivalent material parameters was using the ANSYS optimization package. With the reference data of the segmental lining, the adjusted values of material coefficients are obtained via reverse reconstruction of the first three natural frequencies of the equivalent lining based on response surface model. Lastly, with the adjusted values, the equivalent lining deformation under various load conditions was simulated. Fig. 11 shows the relationships of the structural deformations vs. loads, with the optimization process of the material parameters, the equivalent lining predicts the structural deformation fairly well with the segmental lining.

The values of material parameters are listed in Table 1, where E_r, E_θ and E_z represent elastic constants, $V_{r\theta}$, V_{rz} and $V_{\theta z}$ represent Poisson's ratio; $G_{r\theta}$, $G_{\theta z}$ and G_{zr} represent shear modulus; the subscripts r, θ and z are the directions based on cylindrical coordinates. The initial values are derived from the lining reduction simulations, and the adjusted values are obtained by the optimization process of material parameters for the

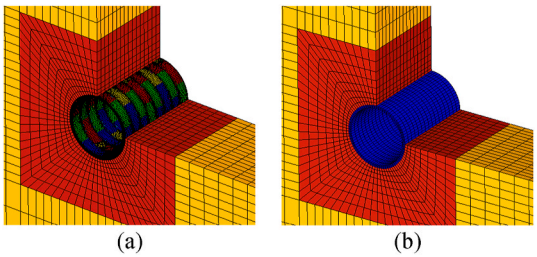

Fig. 10. Lining models: (a) segmental lining model, (b) equivalent lining model.

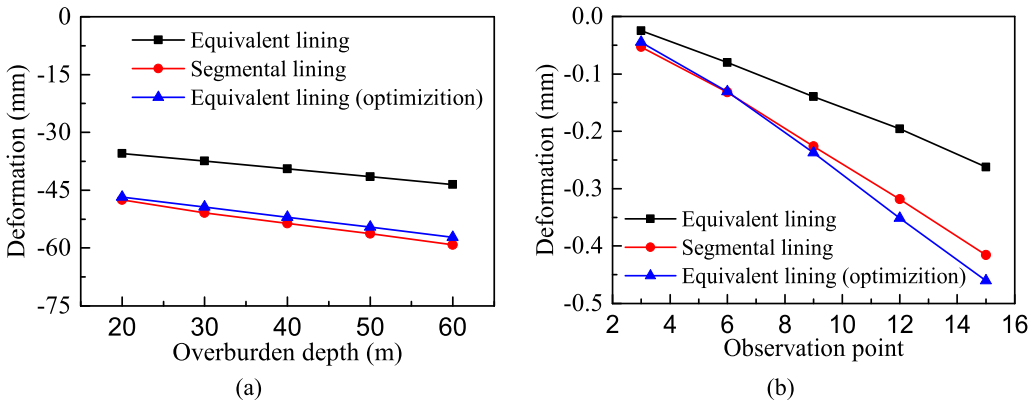

Fig. 11. Relationships between deformation and loads: (a) overburden load, (b) longitudinal load.

Table 1
Main material parameters after the optimization process.

Parameters	Initial values	Adjusted values
E_r (GPa)	24.5	20.8
$V_{r\theta}$	0.2	0.23
E_θ (GPa)	24.5	23.9
$G_{r\theta}$ (GPa)	10.9	11.7
E_z (GPa)	18.4	18
V_{rz}	0.2	0.04
$V_{\theta z}$	0.2	0.21
$G_{\theta z}$ (GPa)	6.1	6.04
G_{zr} (GPa)	6.1	5.98

equivalent lining model.

Fig. 12 provides a comparison of the mode shapes and vibration frequencies between lining models. It can be concluded that the concerned mode shapes and natural frequencies of the equivalent lining produce a good correlation with that of the segmental lining.

3.3. Validation of a tunnel-soil model

Since the subway vehicle passes in close proximity of a physics laboratory where equipment is sensitive to ground variations, the ground response analysis of line 4 of the Beijing metro comes into sight of scholars [26,27], especially for subway induced variations near the northern side of the Chengfulu Station. In 2007, Gupta et al. [26] developed a coupled periodic FE-BE model to simulate the ground variation generated by the subway line. And the same problem was analyzed by Hung et al. [27], using the 2.5D approach Considering the effect of rail irregularity. In order to validate the numerical method of a tunnel-soil system, a 3D finite element model is established in terms of the experiment given by Gupta et al. [26] and the simulation proposed by Hung et al. [27]. The schematic of the soil-tunnel system and observation point is shown in Fig. 13. The material parameters of the soil, tunnel and track parameters are listed in Table 2, where E is Yang's modulus, ν is Poisson's ratio, ρ is mass density, and β is the damping ratio.

Fig. 14 shows the finite element model of the tunnel-soil system. The rigid bodies of the train are established, consisting of 6 carriages with a total length of 116 m. The FRA track irregularity Grade 1 is introduced to model the poorest quality of the rail and the corresponding parameters are derived from Hung et al. [27]. The soil-tunnel system is subjected to the excitation due to the train passing through the observation point. Non-reflecting boundaries are defined as a collection of segments, and segments are equivalent to element faces on the boundary. Non-reflecting boundaries are used on the exterior boundaries of an analysis model of an infinite domain, to prevent artificial stress wave reflections generated at the model boundaries from reentering the model and contaminating the results. Moreover, the viscoelastic boundary was assigned on the surrounding boundary of the three-dimensional finite element model. It can be regarded as a series of spring damping elements. During the implementation process of artificial boundary, an exterior layer of elements was modeled around the soil model, and the material parameters are consistent with that of the original soil layer connected to it, except for the elastic modulus of the viscoelastic boundary. Then, fixed constraint was assigned on the artificial

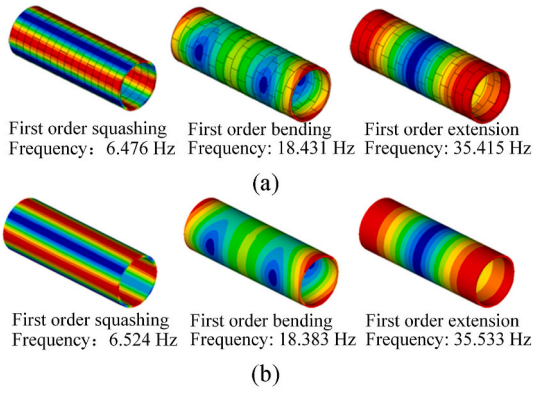

Fig. 12. Mode shapes and natural frequencies: (a) segmental model, (b) equivalent model.

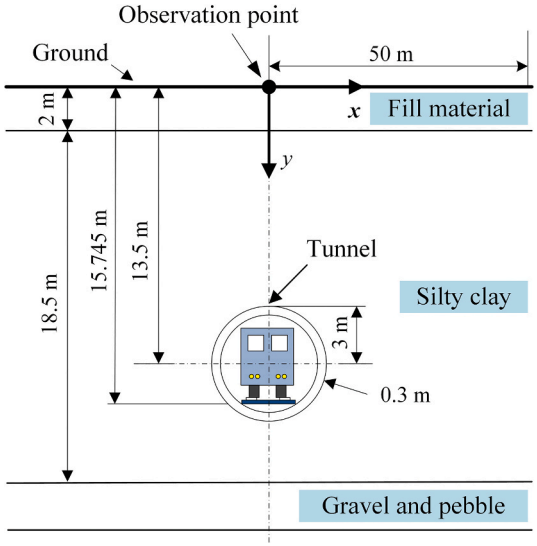

Fig. 13. Schematic of soil-tunnel system and observation point.

Table 2
Material parameters for the soil-tunnel model.

Material	E (MPa)	ν	ρ (kg/m^3)	β
Concrete lining	35000	0.25	2500	0.02
Concrete slab	28500	0.2	2500	0.02
Foundation	0.5	0.25	150	0.1
Fill material	116.6	0.341	1900	0.05
Silty clay	289	0.313	2023	0.04
Gravel and pebble	704	0.223	1963	0.03

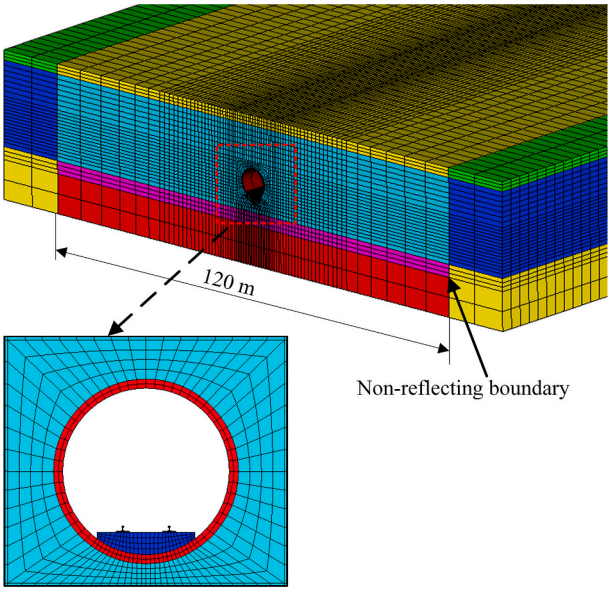

Fig. 14. Finite element model of the tunnel-soil system.

boundary. The elastic modulus of the viscoelastic boundary is determined by

$$E' = \frac{h}{r_b} E \tag{13}$$

Where E' and E represent elastic modulus of the viscoelastic boundary and the original soil layer, respectively. Variable h is the distance between the wave source and the extended soil layer, and r_b represents the element thickness of the extended soil layer.

Fig. 15 indicates time histories of acceleration and displacement responses on the observation point. With respect to the dynamic response of observation point subjected to moving train excitation, the peak value of the acceleration time history derived from the present simulation agrees well with that given by Hung et al. [27]. For lack of exact information of track irregularities, the magnitude of displacement on the observation point has little difference with that in the case of the simulation proposed by Hung et al. [27], which are 0.095 mm and 0.088 mm, respectively. As can be seen, the time histories of dynamic response calculated in this paper show good correlation with that by Hung et al. [27].

4. Numerical model of the train-tunnel-soil system

4.1. Train modeling

4.1.1. Train model details

Fig. 16 shows the metro train of Nanjing Metro Line 10. The subway vehicle consists of six carriages which a car body, two bogies, four wheel sets and four spring-dashpot systems are attached to.

Fig. 17 indicates the dynamic analysis model of the carriage body. The subway train modeled by multi rigid-bodies connected with spring-dashpot relationships, and the interaction between wheel and rail is defined as a penalty contact algorithm. The following conditions are assumed during the modeling procedure:

(1) As the assumption has been validated by Xia et al. [14,28], the elastic deformations of the carriages, bogies, and wheel sets can be neglected, and these components are considered as rigid bodies.
(2) The model of a single carriage includes five degrees of freedom to describe the translational and rotational displacements of the train carriage. The translation of the carriage involves lateral and vertical displacement, and the rotation of the carriage covers roll, yaw and pitch displacement, respectively. The pitch displacement of the wheel set is neglected.

Fig. 16. Subway vehicle of Nanjing Metro Line 10.

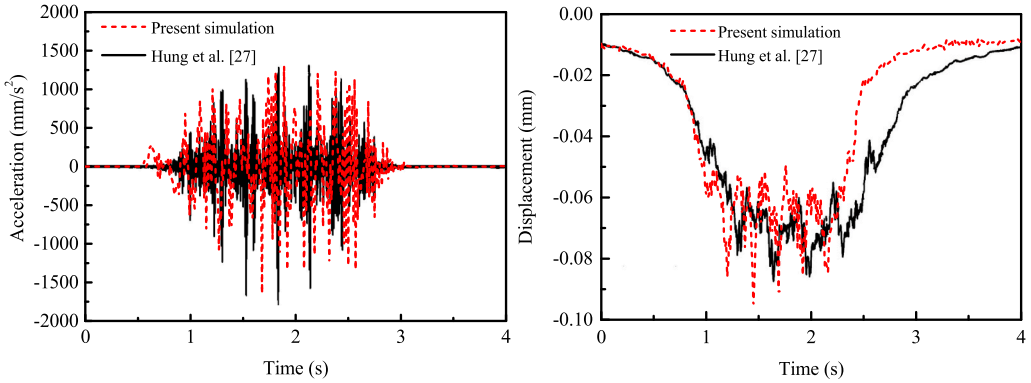

Fig. 15. Validation of dynamic response on the observation point.

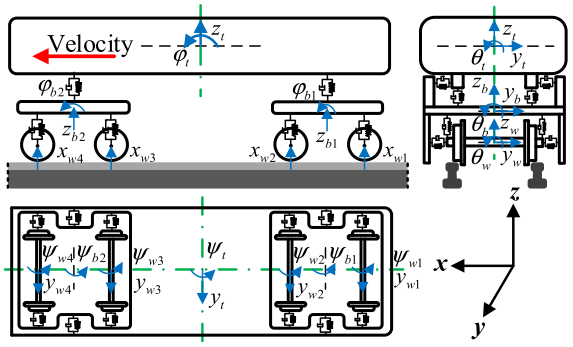

Fig. 17. Dynamic analysis model of a rail vehicle.

(3) Multi rigid-bodies are connected with viscous dashpots and linear springs.
(4) A penalty method is used to constrain the wheel nodes to slide along the track., and the elastic deformation of the rail is neglected.
(5) As the continuity of the track structure is composed of rail slabs, the roughness of the track is considered as a principal vibration to predict the relative displacement between wheel-sets and rails.

Fig. 18 shows the FE model of the subway vehicle based on the assumption above, and the main parameters of the subway vehicle are listed in Table 3.

4.1.2. Track irregularities

The irregularities of the track are regarded as a primary source of excitation. In this work, the roughness of the rail is obtained based on the American standard of railway vehicles [29].

$$S_v(\Omega) = \frac{kA_v\Omega_c^2}{\Omega^2\left(\Omega^2+\Omega_c^2\right)} \tag{14}$$

$$S_a(\Omega) = \frac{4kA_v\Omega_c^2}{\left(\Omega+\Omega_c{}^2\right)\left(\Omega^2+\Omega_s^2\right)} \tag{15}$$

Where $S_v(\Omega)$ and $S_a(\Omega)$ represent the vertical and lateral irregularities; Ω represents the spatial frequency; A_v represents the coefficient related to the line grade; Ω_c and Ω_s denote the cutoff frequencies; and k denotes safety factor.

In this paper, the coefficients of Grade-6 track irregularities are used, which Ω_c, Ω_s, A_v and k are equal to 0.8245 rad/m, 0.4380 rad/m, 0.0339 cm^2 rad/m and 0.25, respectively. Typical samples of random track irregularity (the profiles of the vertical and lateral irregularities) are generated using the method proposed by Gupta et al. [26], as illustrated in Fig. 19.

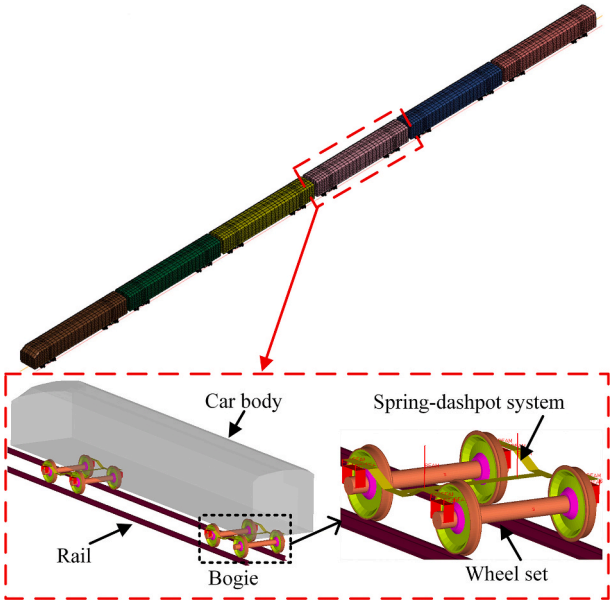

Fig. 18. Finite element model of the railway vehicle.

Table 3
Main parameters for the train vehicle.

Parameters	Value
Carriage length (m)	22.80
Carriage width (m)	3.10
Distance between bogies (m)	12.60
Distance between wheel sets (m)	2.00
Wheel diameter (m)	0.84
Carriage mass (kg)	46,564
Roll inertia of the carriage (kg·m^2)	55,810
Pitch inertia of the carriage (kg·m^2)	1,707,250
Yaw inertia of the carriage (kg·m^2)	1,667,979
Bogie mass (kg)	2418
Roll inertia of the bogie (kg·m^2)	865
Pitch inertia of the bogie (kg·m^2)	3426
Yaw inertia of the bogie (kg·m^2)	2000
Wheel-set mass (kg)	1150
Wheel-set roll inertia (kg·m^2)	726

4.2. Tunnel-soil modeling

According to the geological survey and design materials of Nanjing Metro Line 10, an equivalent finite element model of the tunnel-soil system is established. The detailed description of the tunnel-soil model is indicated in Fig. 20. The tunnel-soil model is made up of eight-noded elements, discretized by brick and thick shell types. In order to eliminate the insufficient accuracy and the low-frequency shift instability caused by the viscous boundaries in the simulation of infinite domains. During the process of numerical simulation, the viscoelastic boundary was applied around the soil model, as can be seen in Fig. 20b. The elastic modulus of the viscoelastic boundary is determined by Eq. (13), and the other material properties are consistent with that of the corresponding soil layer. Meanwhile, non-reflecting boundaries were applied on the exterior boundaries for a simulation of an infinite domain.

Considering the computational efficiency and the accuracy of soil-tunnel contact calculation, the determination of element size is mainly based on the experience of numerical analysis. The soil model is split

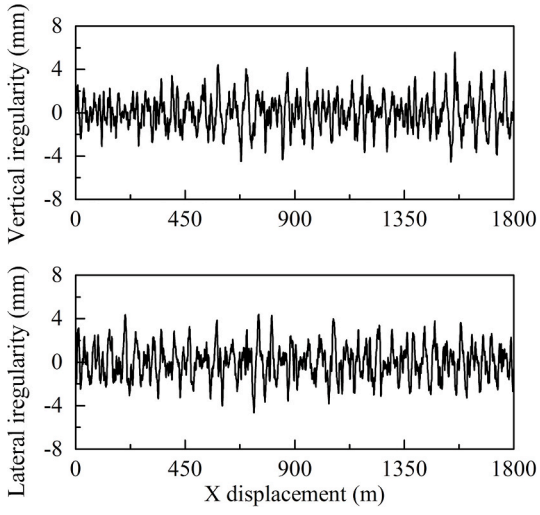

Fig. 19. Time sequence profiles of track irregularities.

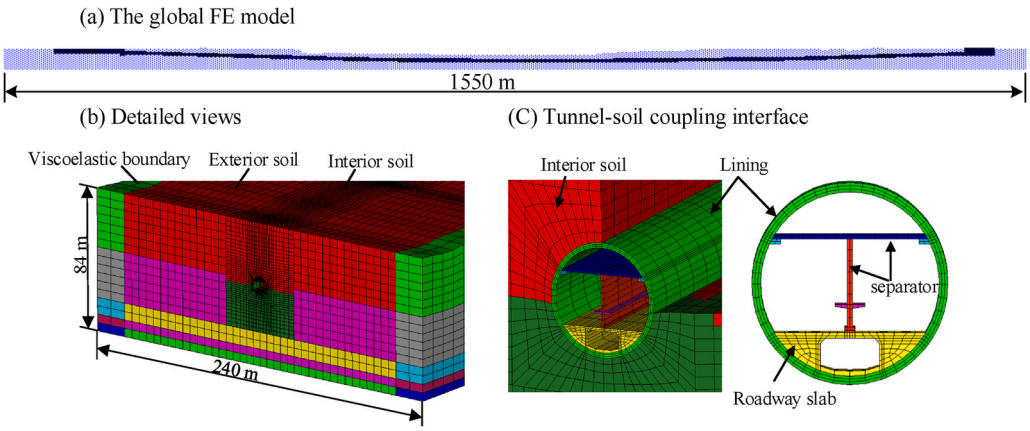

Fig. 20. Tunnel-soil interacted FE model.

into interior soil and exterior soil using different mesh densities. The relationship between interior soil and exterior soil was associated with the contact algorithm. With respect to the thickness of elements, it should meet the following constraints [25].

$$h_{\max} = \left(\frac{1}{5} \sim \frac{1}{8}\right)\lambda = \left(\frac{1}{5} \sim \frac{1}{8}\right)\frac{c}{f_{\max}} \tag{16}$$

where h_{max} represents the thickness of elements. Variables λ, c and f_{max} are the wavelength, velocity and maximum frequency of shear wave in the soil layer, respectively. In this study, six elements per wavelength were adopted for the simulation model. Thus, the minimum element size of the soil-tunnel model was 2.5 m, located at the separator structure of the tunnel lining. The corresponding timestep is equal to 2.01E-5 s. The FE model of the soil-tunnel system consists of 2,320,222 nodes and 2,039,036 elements.

The subway tunnel structure is discretized by the thick shell elements. The surface to surface contact is applied to capture the interaction relationship between tunnel and soil. Four observation points are defined at the cross section to extract the vibration response of the underground subway tunnel, and two typical cross section were defined, as shown in Fig. 21.

The soil model is established in accordance with actual geological characteristics, and soil layers are composed of different materials using different size of solid elements. As illustrated in Fig. 22, the specific sections of the tunnel lining structure are surrounded with completely different soil layers.

In order to better estimate the frictional resistance and the dilation angle of the rock and the soil, the modified Drucker-Prager model (*MAT_DRUCKER_PRAGER) was incorporated in the LS-DYNA program. It enables the shape of the yield surface to be distorted into a more realistic definition for soils. Viscoelastic artificial conditions are applied to the surrounding of the finite element model [30,31]. The Rayleigh damping model, where the damping is defined as a combination of mass proportional and stiffness proportional damping, is adopted for the track-tunnel-soil interaction sub-model [32]:

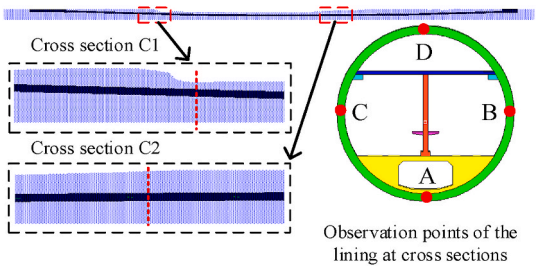

Fig. 21. Description of tunnel observation points at cross sections.

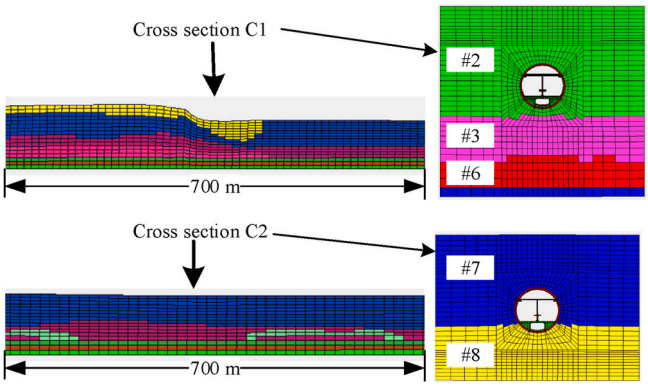

Fig. 22. Description of the soil layers surrounding the tunnel.

$$\mathbf{C} = \alpha\mathbf{M} + \beta\mathbf{K} \tag{17}$$

Where **C, M** and **K** represent the damping, mass and stiffness matrixes, respectively; α and are proportional damping coefficients of mass and stiffness, respectively, and coefficients of α and β can be determined by Ref. [33]:

$$\alpha = \frac{2\omega_1\omega_2}{\omega_1 + \omega_2}\xi, \quad \beta = \frac{2}{\omega_1 + \omega_2}\xi \tag{18}$$

Where ξ is the damping ratio of soil; parameters ω_1 and ω_2 represent the first and second natural frequencies, respectively. The material parameters of rock and soil are listed in Table 4, where ρ is density of the soil layer, V is Poisson's ratio, C is the Cohesion and E represents the elastic constant.

Table 4
Material parameters of rock and soil.

Layer number	ρ (kg/m^3)	V	C (KPa)	ϕ (°)	E (MPa)	α	β
#1	1825	0.26	9.0	28.0	60	0.415	0.0097
#2	1846	0.36	12.1	10.5	40.2	0.394	0.0087
#3	1796	0.30	4.2	10.5	68.2	0.482	0.0135
#4	1836	0.28	8.3	25.5	98.8	0.465	0.0142
#5	1836	0.32	18.2	18.0	125.7	0.293	0.0059
#6	1822	0.28	18.4	30.0	184.3	0.356	0.0074
#7	1977	0.26	16.5	30.0	182.4	0.332	0.0081
#8	1959	0.24	12.3	35.0	343.7	0.315	0.0076
#9	1760	0.35	0	35.0	692	0.251	0.0037
#10	2040	0.42	26.4	28.0	1443.7	0.206	0.0014
#11	2630	0.35	0	35.0	3834.4	0.242	0.0016
#12	2600	0.42	26.4	28.0	11268.5	0.162	0.0010

4.3. Seismic loads

An actual observed seismic acceleration in Shanghai (see Fig. 4) is represented as the earthquake excitation in the present simulation. In terms of the code for seismic design of urban rail transit structures [34] in China, the seismic intensity at the underground structure site is 7° in accordance with the basic design ground motion acceleration of 0.1 g. Therefore, the peak value of the acceleration for the seismic wave is normalized to 0.1 g. Seismic loads were assigned on a collection of nodes located at the bottom surface of the lowest soil layer. The present analysis only takes the shear wave into account, and thus the seismic acceleration is in the lateral direction (along the coordinate axis in Y direction).

5. Results and discussion

5.1. Dynamic response of the tunnel lining

5.1.1. Effect of various excitation conditions

As the underground tunnel structure is deeply immersed, the tunnel lining structure is subject to the gravity of the soil, resulting in the initial stress and deformation. For this reason, the dynamic relaxation method is adopted to assign the initial state of the train-tunnel-soil system before the dynamic response simulation. Fig. 23 illustrates the vertical-displacement and stress-response time histories at the cross-section C1 when the metro train is traveling in the tunnel at a constant speed of 90 km/h. The maximum vertical displacement of the tunnel is 0.91 mm, and the maximum stress fluctuation of the tunnel is about 0.13 MPa.

Time histories of the dynamic response of the subway tunnel during earthquakes are indicated in Fig. 24. It is obviously observed that the maximum vertical displacement of the tunnel is 20.87 mm, while there is little difference between the four measured points. The maximum stress fluctuation of the tunnel is about 2 MPa at the measured points B and C. It is concluded that in contrast to the train moving, the earthquake had great effects on the dynamic response of tunnel structure.

5.1.2. Effect of various soil conditions

Under a load of moving train, the vertical displacement and stress response of observation points for section C1 of the lining are almost consistent with that of section C2. Therefore, only the measured points A and B are introduced to the dynamic response time histories, as indicated in Fig. 25.

Fig. 26 shows the lateral displacement at different lining sections due to earthquake action. With respect to the trough at 3.9 s, the trough level at lining section C1 is equal to 39.93 mm, 32.48% more than the corresponding value of 30.14 mm at lining section C1. Regarding the maximum peak, the peak value of lateral displacement at lining section C1 is 26.03 mm, with a percentage of 17.25% more than the peak value of 22.20 mm at section C2. It is found that the seismic excitation has a significant impact on the peak value of the lateral displacement of lining sections under different soil conditions. Furthermore, the difference between lateral displacement may sharpen with the increase of seismic intensity, which poses a severe security threat to running safety of subway vehicles.

5.2. Dynamic response of the vehicle

As the metro train passes through the subway tunnel at the designed operational speed of 90 km/h, an earthquake load with a peak acceleration of 0.1 g is applied to the train-tunnel-soil system. The dynamic response of the first carriage is shown in Fig. 27. As the subway vehicle travels in the tunnel at 90 km/h, the peak values of vertical and lateral accelerations are 0.533 m/s^2 and 0.275 m/s^2, respectively. As the subway tunnel is subjected to an earthquake load, the peak values of lateral and vertical accelerations are equal to 0.603 m/s^2 and 0.706 m/s^2, respectively, and the maximum lateral and vertical accelerations of the first car body increase by 13.2%, 256.7%, respectively. It can be seen that the seismic load has a significant effect on the first car-body acceleration at a lateral direction.

Since the lateral force and the vertical force between the wheel and rail is often used to obtain the derailment coefficient, these two forces of the first wheel set are adopted to investigate the force response of the moving subway vehicle. The lateral force is derived from the X-coordinate force of the output force file, while the vertical force represents the Z-coordinate force. As the force histories of the wheels without an earthquake load are illustrated in Fig. 28, with the excitation of track irregularities, the peak value of the left and right wheel-rail forces has no obvious difference but phase difference. Fig. 29 indicates the time histories of the wheel-rail forces with the wheel set subjected to earthquake excitation. It can be obviously observed that the earthquake load has significant effect on the wheel-rail forces.

5.3. Running safety evaluation of moving trains

On the one hand, the running safety of the metro train due to earthquake excitation is assessed. On the other hand, in order to evaluate, the influence of train speed and earthquake loads on the running safety of the subway vehicle during an earthquake is discussed.

5.3.1. Running safety of the train

In general, the safety indices related to derailment factor, offload factor and the wheel-rail force are frequently adopted to assess the running safety of the train vehicle [35,36]. In this section, the evaluation indices for the running safety of the train currently adopted in the metro railways in China were used, and the safety index for the running safety of subway vehicles can be expressed as follows [37]:

$$\begin{aligned} &\text{Derailment factor}: Q/P_1 \le 0.8 \\ &\text{Offload factor}: \Delta P \Big/ \overline{P} \le 0.6 \\ &\text{Wheel}-\text{rail force}: Q \le 0.85(10 + P_{st}/3) \end{aligned} \tag{19}$$

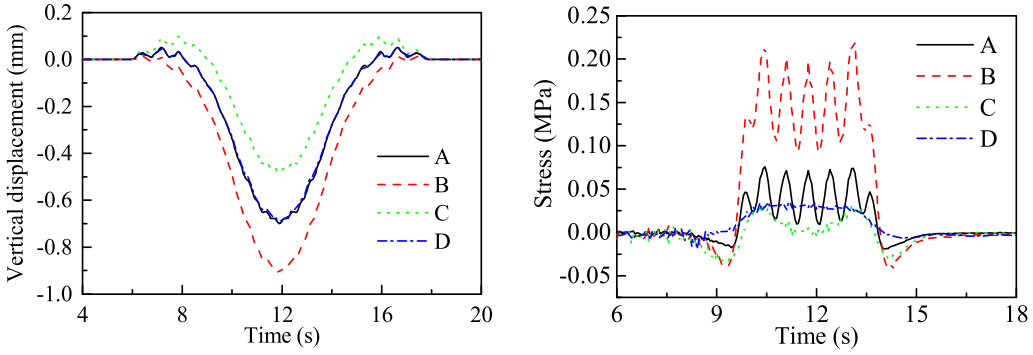

Fig. 23. Dynamic response of tunnel during train moving.

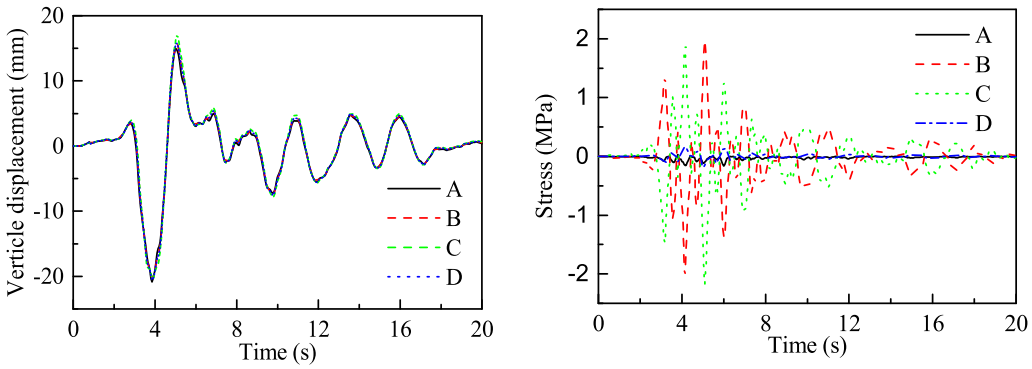

Fig. 24. Dynamic response of tunnel during earthquakes.

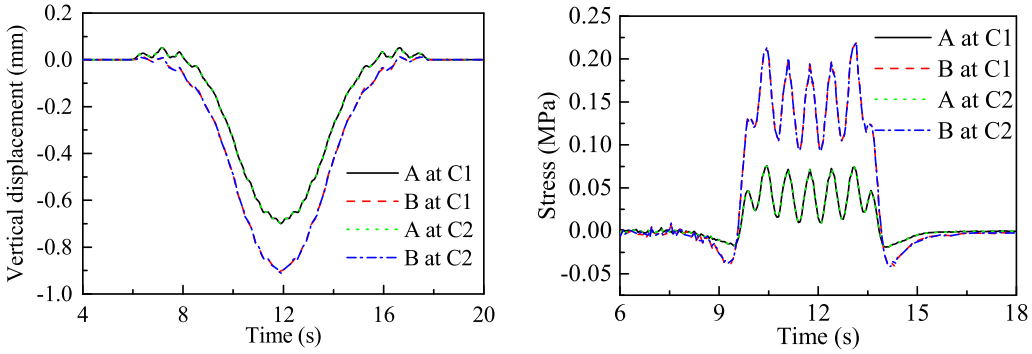

Fig. 25. Dynamic response of different lining sections during train moving.

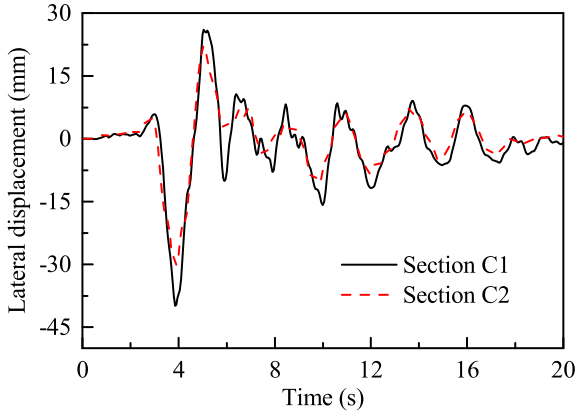

Fig. 26. Lateral displacement of different lining sections under earthquake.

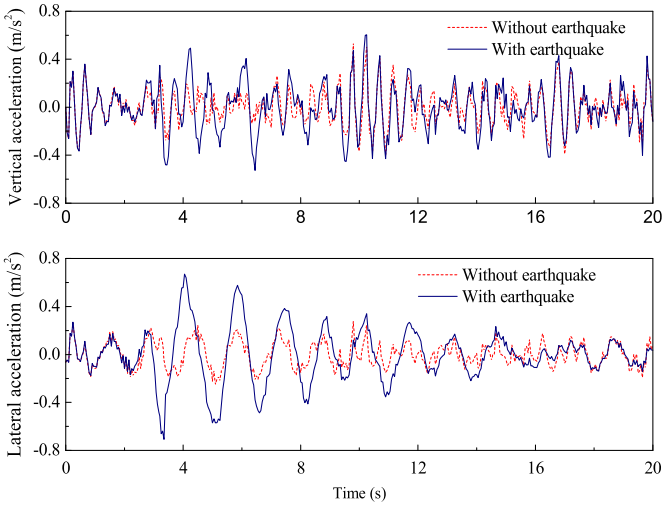

Fig. 27. Time histories of acceleration of the first car-body.

where Q denotes the lateral wheel-rail force; P_1 is the vertical force of the wheel at the climbing-up-rail side; ΔP represents the offload vertical wheel-rail force, and $\overline{P}$ the average vertical wheel-rail force; P_{st} represents the static wheel-rail force.

Derailment factor is an index to evaluate the safety of vehicle wheel against derailment [38]. To study derailment factor and corresponding contact states, a simulation of a wheel-rail model (see Fig. 5) due to earthquake action with an acceleration of 0.3 g was performed. Fig. 30 gives the time history of derailment coefficient of the wheel, while the dotted line means the safety allowance. The contact states between wheel and rail are indicated in Fig. 31. It can be obviously seen that the derailment factor fluctuated violently after the time of 2.0 s, and the derailment coefficient of train exceeded the allowance line for several times during earthquake excitation, but the derailment of wheel set did not occur until 5.0 s in Fig. 31b. At the time of 4.6 s, the derailment coefficient reaches the first peak value of 2.28. According to the traditional standard, the railway wheel is in danger of derailment. However, from the contact state in Fig. 31a, although the wheel set is close to the wheel flange, the wheel set is still within the track limit, and no derailment occurs. It can be seen from Fig. 31b that at 5.0 s, the right wheel flange has almost broken away from the track, but the derailment coefficient is within the safety limit (see Fig. 30). Furthermore, it is worth noting that the derailment coefficient has exceeded the allowance for many times under the seismic loads, but the derailment of vehicle wheel does not occur at the time when the safety index reaches the maximum value.

Fig. 32 shows safety index histories of the subway vehicle subjected

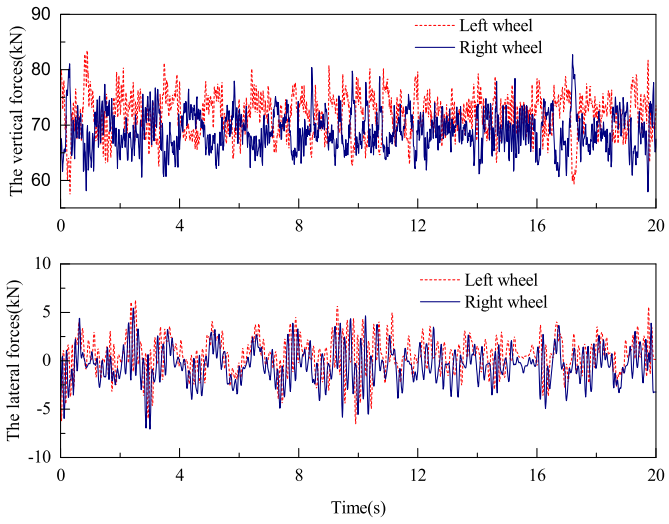

Fig. 28. Wheel-rail force histories of the wheels without earthquake.

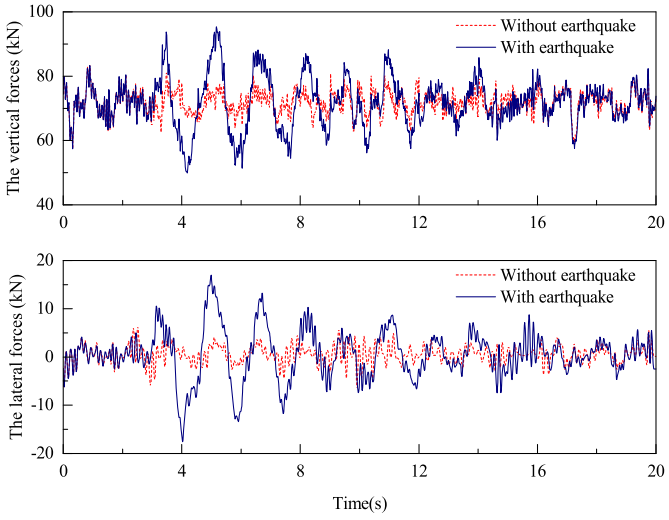

Fig. 29. Time histories of wheel-rail forces due to earthquake action.

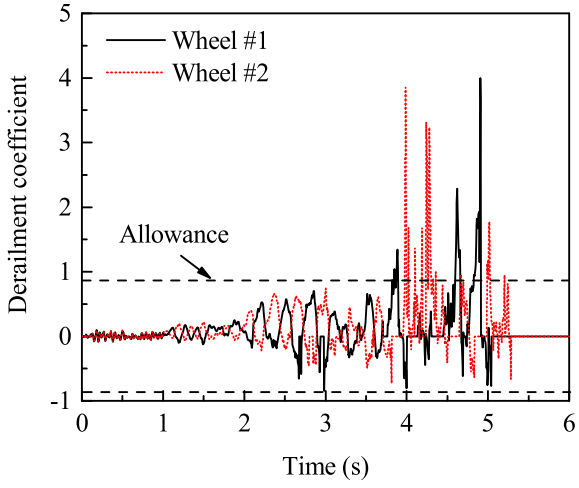

Fig. 30. Derailment coefficient of the wheel set under seismic loads.

to an earthquake load. It is obviously observed that the input earthquake excitation has a significant effect on the safety indices of the moving metro train. As a subway train traveling through the tunnel without an earthquake, the peak value of derailment and offload factors are equal to 0.169 and 0.097, respectively. Subjected to an earthquake load, the running safety indices are obviously enlarged. It is indicated that the magnitude of the derailment factor and the offload factor are 0.353 and 0.323, respectively, and the safety indices increase by 108.9%, 233.0%, respectively. On the other hand, as for the subway train speed of 90 km/h, both the derailment and offload factor are within the safety allowance range respectively as a metro vehicle passes through the underground tunnel structure subjected to a peak acceleration of earthquake excitation equal to 0.1 g.

5.3.2. *Effect of earthquake intensity*

The effect of earthquake intensity on running safety indices of the subway vehicle is indicated in Fig. 33. It is illustrated that the running safety coefficients increase as the maximum acceleration of the earthquake load increases. With respect to the peak acceleration of 0.2 g, the offload coefficient of a subway train with a speed of 100 km/h is out of the safety allowance range. In respect of the peak acceleration of 0.25 g, the derailment coefficient is out of allowance for the metro vehicle at 70 km/h. It is worth noticing that it is safe for the railway vehicle at speed from 70 km/h to 100 km/h to pass through the subway tunnel under an earthquake load with a peak acceleration equal to 0.15 g. It can be found that the earthquake intensity has significant effects on safety index.

5.3.3. *Effect of train speed*

Fig. 34 shows the effect of train speed on derailment and offload factors of moving trains, in which the dash lines represent the Chinese allowable value of safety index [35]. Since the operating speed of the subway is relatively low, as the peak ground acceleration of earthquake excitation is less than or equal to 0.2 g, running safety indices are not sensitive to the change of speed, with the exception of that at the speed of 100 km/h, the offload coefficient of a subway train under the peak ground acceleration of 0.2 g is out of allowance. It can be concluded that the speed has a little effect on safety index with the train under the peak ground acceleration of 0.05 g, 0.1 g and 0.15 g. Meanwhile, it is worth noting that with the increase of earthquake intensity, the influence of vehicle speed on running safety indices increases significantly.

5.3.4. *Running safety evaluation*

Fig. 35 illustrates the response surface of running safety indices. The threshold profile of the running safety index can be obtained by employing the critical points related to corresponding ground acceleration and train speed, as indicated in Fig. 36. In general, as the peak ground acceleration increases, the critical speed decreases obviously. It can be concluded that the critical speed of the metro vehicle decreases with the increase of the peak ground acceleration. In addition, at the design operating speed of 90 km/h for the subway vehicle, the maximum magnitude for the acceleration of an earthquake load is 0.2 g, which the safety indices will not exceed the allowance range.

6. Conclusions

In this paper, a 3D finite element model of the train-tunnel-soil coupled system during earthquakes is established. On the one hand, the explicit algorithm is applied to numerically simulate the dynamic response of the underground tunnel and the subway vehicle. On the other hand, running safety of moving trains in the tunnel during earthquakes is calculated based on the numerical results. Furthermore, the effect of train speed and earthquake intensity on the running safety of the metro train is evaluated. The conclusions are drawn from this paper as follows.

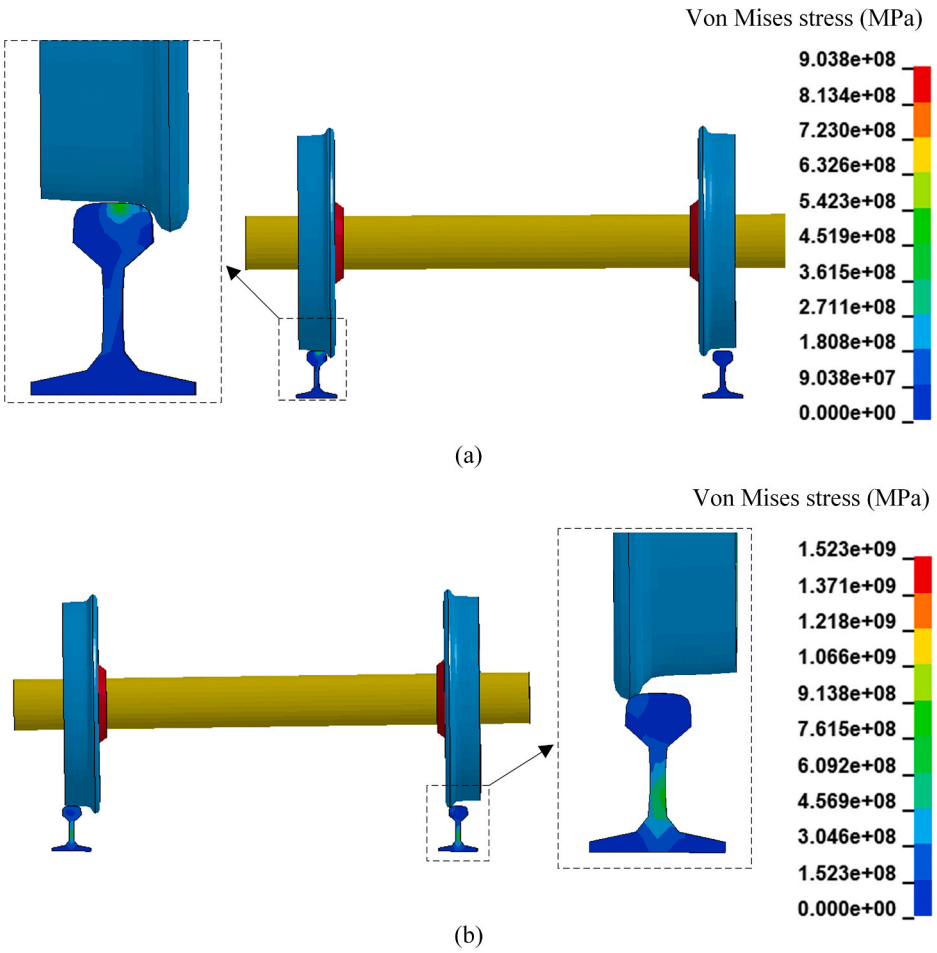

Fig. 31. Wheel-rail contact states. (a) t = 4.6 s. (b) t = 5.0 s.

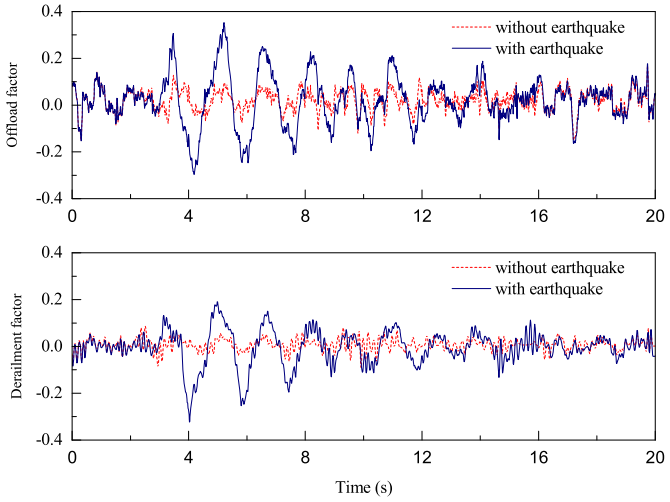

Fig. 32. Time histories of the safety index of the rail vehicle.

(1) The numerical approaches and the tunnel-soil model employed in this work produce a good correlation with the measured vibration test data, which provides an effective way to capture dynamic responses of the subway tunnel and the metro train.
(2) In contrast to the excitation induced by the moving train, the earthquake load has more significant effects on the dynamic response of the Nanjing Metro Line 10 tunnel. Effect of the earthquake on the wheel-rail force and acceleration of the subway vehicle is noticeable as well.
(3) The earthquake load has a significant effect on the running safety indices of the metro vehicle. On the other hand, it is safe for the metro vehicle to pass through the subway tunnel of the Nanjing Metro Line 10 at the designed operating speed of 90 km/h even though the tunnel and the vehicle are subjected to an earthquake load with a peak acceleration of 0.2 g.
(4) Both the intensity of the earthquake and train speed have an impact on the running safety of the subway. It is worth noticing that the earthquake intensity has more significant effects on safety index.
(5) A threshold curve related to the corresponding earthquake intensity and train speed proposed for the Nanjing Metro Line 10 can be employed for the running safety evaluation of the subway train.

Author statement

I have made substantial contributions to the conception or design of the work; or the acquisition, analysis, or interpretation of data for the work; AND.

I have drafted the work or revised it critically for important intellectual content; AND.

I have approved the final version to be published; AND.

I agree to be accountable for all aspects of the work in ensuring that questions related to the accuracy or integrity of any part of the work are appropriately investigated and resolved.

All persons who have made substantial contributions to the work reported

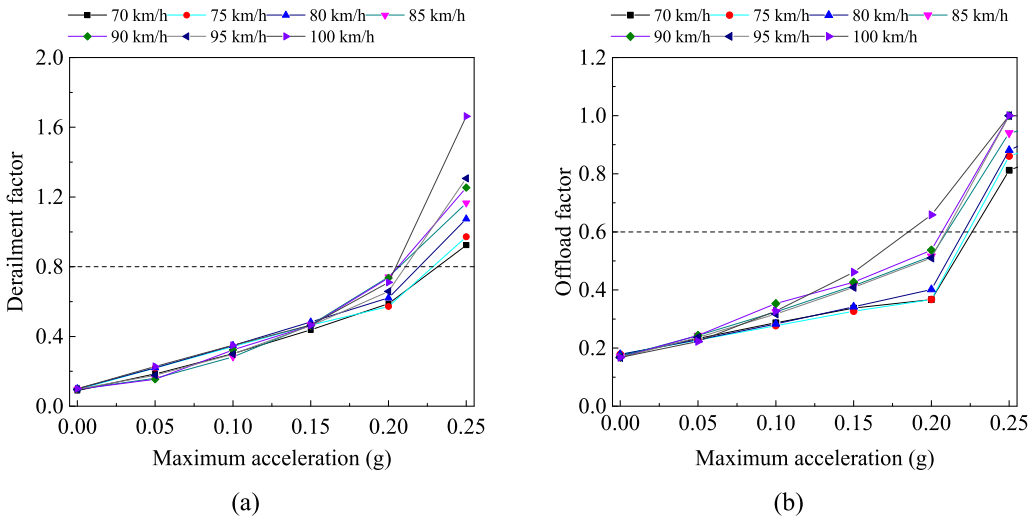

Fig. 33. Influence of earthquake intensity on running safety indices: (a) derailment factor; (b) offload factor.

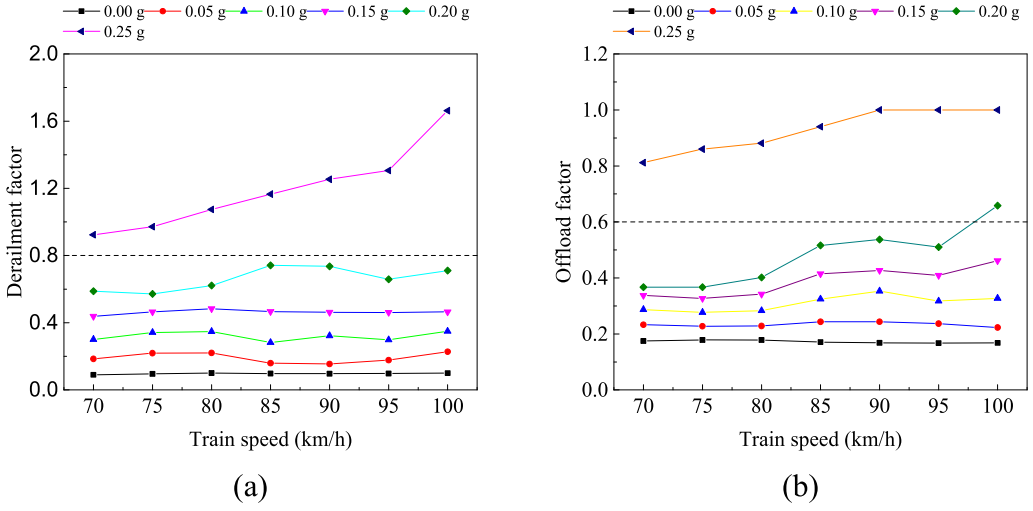

Fig. 34. Influence of train speed on running safety indices: (a) derailment factor; (b) offload factor.

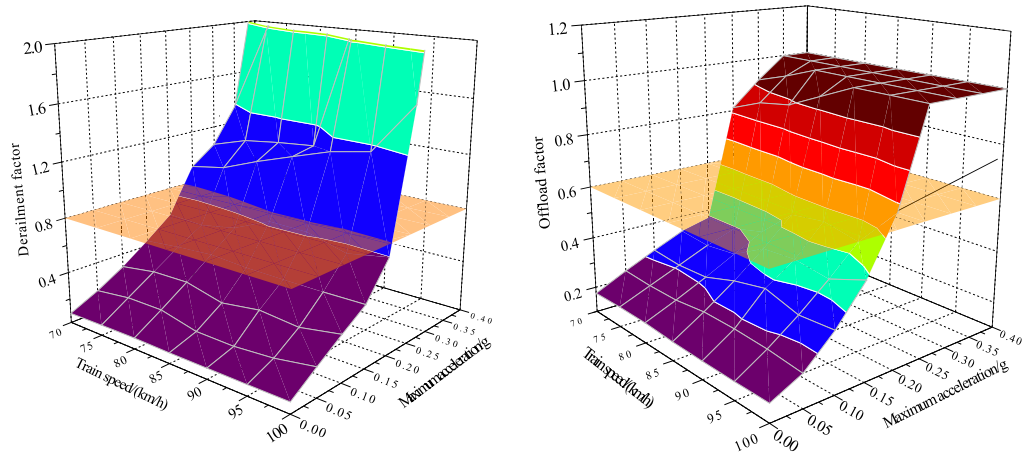

Fig. 35. Response surface of running safety indices: (a) derailment factor, (b) offload factor.

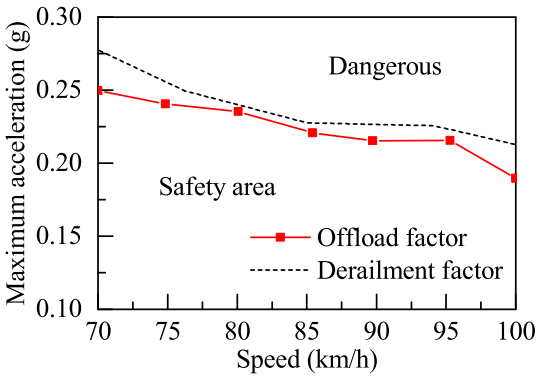

Fig. 36. The threshold profile of critical train speed.

in the manuscript, including those who provided editing and writing assistance but who are not authors, are named in the Acknowledgments section of the manuscript and have given their written permission to be named. If the manuscript does not include Acknowledgments, it is because the authors have not received substantial contributions from non-authors.

Junjie Li: Investigation, Software, Data curation, Writing-Original draft preparation. Yunfeng Lou: Writing-Reviewing and Editing, Visualization. Xun Yang: Investigation, the first idea of the proposed model, Validation, Resources. Xianlong Jin: Conceptualization, Formal analysis, Methodology, Supervision, Funding acquisition.

Declaration of competing interest

The authors declare that they have no known competing financial interests or personal relationships that could have appeared to influence the work reported in this paper.

Acknowledgement

This work was supported by the National Key Research and Development Program of China (Grant no. 2016YFB0201800) and the National Natural Science Foundation of China (Grant no. 11772192).

References

[1] Chen J, Shi X, Li J. Shaking table test of utility tunnel under non-uniform earthquake wave excitation. Soil Dynam Earthq Eng 2010;30(8):1400–16.
[2] Anastasopoulos I, Gerolymos N, Drosos V, Kourkoulis R, Georgarakos P, Gazetas G. Nonlinear response of deep immersed tunnel to strong seismic shaking. J Geotech Geoenviron Eng 2007;133(9):1067–90.
[3] Hatzigeorgiou GD, Beskos DE. Soil-structure interaction effects on seismic inelastic analysis of 3-d tunnels. Soil Dynam Earthq Eng 2010;30(9):851–61.
[4] Gomes RC, Gouveia F, Torcato D, Santos J. Seismic response of shallow circular tunnels in two-layered ground. Soil Dynam Earthq Eng 2015;75:37–43.
[5] Do NA, Dias D, Oreste P, Irini DM. 2D numerical investigation of segmental tunnel lining under seismic loading. Soil Dynam Earthq Eng 2015;72:66–76.
[6] Do NA, Dias D, Oreste P, Djeran-Maigre I. Behaviour of segmental tunnel linings under seismic loads studied with the hyperstatic reaction method. Soil Dynam Earthq Eng 2015;79:108–17.
[7] Fabozzi S, Bilotta E. Behaviour of a segmental tunnel lining under seismic actions. Procedia engineering 2016;158:230–5.
[8] Degrande G, Clouteau D, Othman R, Arnst M, Chebli H, Klein R, Chatterjee P, Janssens B. A numerical model for ground-borne vibrations from underground railway traffic based on a periodic finite element-boundary element formulation. J Sound Vib 2006;293(3–5):645–66.
[9] Galvin P, Francois S, Schevenels M, Bongini E, Degrande G, Lombaert G. A 2.5D coupled FE-BE model for the prediction of railway induced vibrations. Soil Dynam Earthq Eng 2010;30(12):1500–12.
[10] Gupta S, Van den Berghe H, Lombaert G, Degrande G. Numerical modelling of vibrations from a Thalys high speed train in the Groene Hart tunnel. Soil Dynam Earthq Eng 2010;30(3):82–97.
[11] Andersen L, Jones C. Coupled boundary and finite element analysis of vibration from railway tunnels-a comparison of two-and three-dimensional models. J Sound Vib 2006;293(3):611–25.
[12] Tanabe M, Matsumoto N, Wakui H, Sogabe M, Okuda H. A simple and efficient numerical method for dynamic interaction analysis of a high-speed train and railway structure during an earthquake. J Comput Nonlinear Dynam 2008;3(4):1896–905.
[13] Ju SH. Improvement of bridge structures to increase the safety of moving trains during earthquakes. Eng Struct 2013;56(6):501–8.
[14] Xia CY, Xia H, De Roeck G. Dynamic response of a train–bridge system under collision loads and running safety evaluation of high-speed trains. Comput Struct 2014;140:23–38.
[15] Yang X, Wang H, Jin X. Numerical analysis of a train-bridge system subjected to earthquake and running safety evaluation of moving train. Shock Vib 2016;2016. https://doi.org/10.1155/2016/9027054.
[16] Guo Y, Jin X, Ding J. Parallel computing for seismic response analysis of immersed tunnel with domain decomposition. Eng Comput 2007;24(2):182–99.
[17] Ding J, Jin X, Guo Y, Li G. Numerical simulation for large-scale seismic response analysis of immersed tunnel. Eng Struct 2006;28(10):1367–77.
[18] Hallquist JO. LS-DYNA theory manual. Livermore, CA: Livermore Software Technology Corporation; 2007.
[19] Hallquist JO. LS-DYNA keyword user's manual. Livermore, CA: Livermore Software Technology Corporation; 2007.
[20] Bosso N, Spiryagin M, Gugliotta A, Somà A. Contact model. In: Mechatronic modeling of real-time wheel-rail contact. Berlin, Heidelberg: Springer; 2013.
[21] Kalker JJ. Three-dimensional elastic bodies in rolling contact. Dordrecht: Kluwer Academic Publishers; 1990.
[22] Ayasse JB, Chollet H. Determination of the wheel rail contact patch for semi-Hertzian conditions. Veh Syst Dyn 2005;43(3):159–70.
[23] Ju SH. A frictional contact finite element for wheel/rail dynamic simulations. Nonlinear Dynam 2016;85(1):365–74.
[24] Luo C, Yang X, Zhan C, Jin X, Ding Z. Nonlinear 3D finite element analysis of soil-pile-structure interaction system subjected to horizontal earthquake excitation. Soil Dynam Earthq Eng 2016;84:145–56.
[25] Wang J. Numerical simulation method and application of vehicle-tunnel dynamic coupling system. Doctoral thesis. Shanghai, China: Shanghai Jiao Tong University; 2012.
[26] Gupta S, Liu WF, Degrande G, Lombaert G, Liu WN. Prediction of vibrations induced by underground railway traffic in Beijing. J Sound Vib 2008;310(3):608–30.
[27] Hung HH, Chen GH, Yang YB. Effect of railway roughness on soil vibrations due to moving trains by 2.5 D finite/infinite element approach. Eng Struct 2013;57:254–66.
[28] Xia H, Zhang N. Dynamic analysis of railway bridge under high-speed trains. Comput Struct 2005;83(23–24):1891–901.
[29] Xia H, Zhang N, Guo W. Vibration criteria for HSR bridges and train vehicles in China. In: Dynamic interaction of train-bridge systems in high-speed railways. Advances in high-speed rail technology. Berlin, Heidelberg: Springer; 2018.
[30] Gu Y, Liu J, Du Y. 3-D consistent viscous-spring artificial boundary and viscous-spring boundary element. Eng Mech 2007;28(9):1070–5.
[31] Nakamura N. Nonlinear response analyses of a soil-structure interaction system using transformed energy transmitting boundary in the time domain. Soil Dynam Earthq Eng 2009;29(5):799–808.
[32] Xu Q, Ou X, Au FTK, Lou P, Xiao Z. Effects of track irregularities on environmental vibration caused by underground railway. Eur J Mech Solid 2016;59:280–93.
[33] Leitão FN, Silva JGS, Andrade SAL. Fatigue analysis and life prediction of composite highway bridge decks under traffic loading. Lat Am J Solid Struct 2013;10(3):505–22.
[34] MRC. Code for seismic design of urban rail transit structures. *GB50909-2014*. Beijing, China: China Planning Press; 2014.
[35] Ishida H, Matsuo M. Safety criteria for evaluation of railway vehicle derailment. Quarterly Report of RTRI 1999;40(1):18–25.
[36] Eom BG, Lee HS. Assessment of running safety of railway vehicles using multibody dynamics. Int J Precis Eng Manuf 2010;11(2):315–20.
[37] MRC. Railway vehicle specification for evaluation of dynamic performance and accreditation test. *GB5599-85*. Beijing, China: China Planning Press; 1985.
[38] Xia H, Zhang N, Guo W. Dynamic interaction of train-bridge systems in high-speed railways. Beijing, China: Beijing Jiaotong University Press and Springer-Verlag GmbH Germany; 2018.